HgCdTe-based quantum cascade lasers operating in the GaAs phonon Reststrahlen band predicted by the balance equation method

DMITRII USHAKOV,[1,5] ALEXANDER AFONENKO,[1] RUSTAM KHABIBULLIN,[2,6] DMITRY PONOMAREV,[2] VLADIMIR ALESHKIN,[3,4] SERGEY MOROZOV,[3,4] AND ALEXANDER DUBINOV[3,4]

[1]*Belarusian State University, Minsk 220030, Belarus*
[2]*V.G. Mokerov Institute of Ultra High Frequency Semiconductor Electronics, Russian Academy of Sciences, Moscow 117105, Russia*
[3]*Institute for Physics of Microstructures, Russian Academy of Sciences, Nizhny Novgorod 603950, Russia*
[4]*Lobachevsky State University of Nizhny Novgorod, Nizhny Novgorod 603950, Russia*
[5]*ushakovdv@bsu.by*
[6]*khabibullin@isvch.ru*

Abstract: The lack of radiation sources in the frequency range of 7-10 THz is associated with strong absorption of the THz waves on optical phonons within the GaAs Reststrahlen band. To avoid such absorption, we propose to use HgCdTe as an alternative material for THz quantum cascade lasers thanks to a lower phonon energy than in III-V semiconductors. In this work, HgCdTe-based quantum cascade lasers operating in the GaAs phonon Reststrahlen band with a target frequency of 8.3 THz have been theoretically investigated using the balance equation method. The optimized active region designs, which are based on three and two quantum wells, exhibit the peak gain exceeding 100 cm^{-1} at 150 K. We have analyzed the temperature dependence of the peak gain and predicted the maximum operating temperatures of 170 K and 225 K for three- and two-well designs, respectively. At temperatures exceeding 120 K, the better temperature performance has been obtained for the two-well design, which is associated with a larger spatial overlap of weakly localized lasing wavefunctions, as well as, a higher population inversion. We believe that the findings of this work can open a pathway towards the development of THz quantum cascade lasers featuring a high level of optical gain due to the low electron effective mass in HgCdTe.

1. Introduction

Over the past decade, the significant development of radiation sources covers a wide range of electromagnetic spectrum between mid-infrared (mid-IR) and terahertz (THz) frequencies. One of the reasons for this is a dramatic improvement of quantum cascade lasers (QCLs) performance across the far-IR and THz ranges [1]. On the high-frequency side (10-30 THz), QCLs based on InAs/AlSb [2] and InGaAs/GaAsSb [3] materials have demonstrated the longest wavelengths of 25 μm and 28 μm, which correspond to frequencies of 12.0 THz and 10.7 THz, respectively. On the low-frequency side (1-6 THz), the highest operation frequency of 5.4 THz has been achieved by QCL based on GaAs/AlGaAs [4]. However, the operation of QCLs based on the above-mentioned materials in the frequency range between 7 to 10 THz is strongly affected by the optical phonon absorption in the Reststrahlen band [5]. In particular, the extending of GaAs/AlGaAs QCL operation frequencies above 6 THz results in a significant increase of waveguide propagation loss due to a strong electron-phonon scattering in the GaAs phonon Reststrahlen band [6,7], covering 7-10 THz [8]. For the same reason, it is a challenge for far-IR QCLs to operate at frequencies below 12 THz because of AlAs phonon Reststrahlen band [3].

Thus, one should employ alternative materials with lower or higher optical phonon energies than in GaAs, or utilize non-polar materials , such as GeSi [9], in which the interaction with optical phonons is suppressed [10], as materials for QCLs lasing in the GaAs phonon Reststrahlen band.

Semiconductors with large optical phonon energies, such as GaN or ZnO, are extremely promising materials for THz QCLs with the potential to achieve room temperature operation [11,12]. However, wide-bandgap materials have a higher electron effective mass m_e^* and, therefore, a lower optical gain [13], since $g \sim \left(m_e^*\right)^{-3/2}$. Furthermore, it should be noted that low m_e^* materials like InAs, InSb or GaSb theoretically provide higher optical amplification, but these materials are not suitable for QCLs lasing in a frequency range of 7-10 THz due to their optical phonon energy close to the GaAs one [see Fig. 1]. In contrast to III-V semiconductors, II-VI materials, in particular, $Hg_{1-x}Cd_xTe$ have a lower optical phonon energy than GaAs and simultaneously low values of m_e^*, which makes them attractive for the gap of 7-10 THz [14] . For narrow-gap $Hg_{1-x}Cd_xTe$ with cadmium content less than 60 %, the electron effective mass is comparable to conventional low m_e^* semiconductors. Since the compound materials HgTe and CdTe are closely lattice matched (the difference in lattice constants less than 0.3 %), it is possible to design a wide variety of multilayer structures based on $Hg_{1-x}Cd_xTe$. Moreover, there is a variety of experimentally demonstrated $Hg_{1-x}Cd_xTe$-based devices such as photodetectors of the mid-IR radiation (see, for example, [15] and references therein) and coherent radiation sources operating with a wavelength of up to 19.5 μm [16,17], that shows the technological maturity of this material. Therefore, these benefits of $Hg_{1-x}Cd_xTe$ suggest that it can be employed for QCLs operating in the GaAs Reststrahlen band.
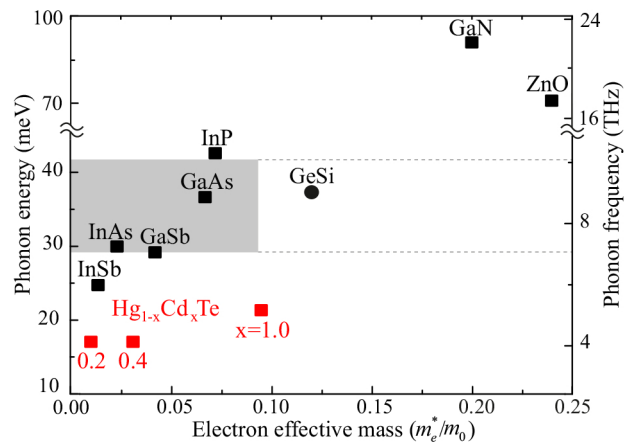
Fig. 1. Summary of candidate materials for QCLs with corresponding electron effective mass and longitudinal optical phonon energy/frequency. Polar semiconductors are indicated by squares and non-polar GeSi is marked by circle. The GaAs phonon Reststrahlen band is indicated by the shaded area.

In this work, to evaluate the potential of $Hg_{1-x}Cd_xTe$ structures as a gain medium for QCL operating in the GaAs phonon Reststrahlen band with a target frequency of 8.3 THz, we use the balance equation method for simulating the laser characteristics. In comparison with widely used approaches for modeling electronic transport in QCLs, such as the nonequilibrium Green's function formalism [18] or the density matrix formalism [19], the balance equation method allows a significant reduction of the computation time. Thus, we have an opportunity to consider a wide variety of active region designs, as well as optimize the given design by varying of the thickness of all layers in the wide range. Moreover, the balance equation method allows us to account the dephasing effect, which clearly plays an important role in QCLs [20,21], and

predicts the formation of electric field domains across the active region [22]. Previously, we have demonstrated the good agreement between calculated and experimental light-current-voltage characteristics for the GaAs/AlGaAs QCL emitting near 2.3 THz [23]. In case of HgCdTe QCLs, it is important to take into account the strong effect of conduction band non-parabolicity in the calculation of electronic states, which is done using the 3-band $\mathbf{k} \cdot \mathbf{p}$ Hamiltonian [24]. In addition, an anomalous temperature dependence of the $Hg_{1-x}Cd_xTe$ band gap (the band gap increases with temperature [15]) is included in our model.

2. Materials and designs

$Hg_{1-x}Cd_xTe$ is a direct-gap compound semiconductor with zinc blende crystal structure, in which the band gap can be varied over a wide range from zero to 1.49 eV by changing the composition [15]. Our choice of the $Hg_{1-x}Cd_xTe/Hg_{1-y}Cd_yTe$ composition for quantum wells/barriers is motivated by the following reasons. On the one hand, the increase of mercury content leads to a decrease in the m_e^*, which is favorable from a theoretical perspective. On the other hand, $Hg_{1-x}Cd_xTe$ with a Hg composition more than 80 % becomes gapless material with a high interband absorption at the target frequency as well as with a detrimental effect of mixing between the states of electrons and holes [25]. Thus, we have used the $Hg_{0.8}Cd_{0.2}Te$ wells as an optimum trade-off between the above-mentioned tendencies. In this case, the bulk effective electron mass of $Hg_{0.8}Cd_{0.2}Te$ is equal to $0.010 \cdot m_0$, where m_0 is a free electron mass. However, the strong effect of non-parabolicity in narrow-gap wells based on $Hg_{0.8}Cd_{0.2}Te$ leads to increasing of effective masses up to $(0.03-0.04) \cdot m_0$, which is still less than in GaAs wells [see Fig. 1].

The target frequency of 8.3 THz requires relatively low values of conduction band offset (less than 500 meV), which can be achieved by the composition of $Hg_{1-x}Cd_xTe$ barrier layers close to composition of $Hg_{0.8}Cd_{0.2}Te$ wells. The height of $Hg_{1-y}Cd_yTe$ barriers is defined as a compromise between the suppression of parasitic leakage current and the difficulties of growth technology. In order to prevent the current leakage into the continuum it is necessary to reduce the Hg content for a higher potential barrier. However, an increase in the conduction band offset results in a decrease in the barrier thickness, creating high requirements on the epitaxial growth. Thus, we prefer $Hg_{0.8}Cd_{0.2}Te/Hg_{0.6}Cd_{0.4}Te$ material system, which provides ~ 289 meV conduction band offset at 50 K and allows designing an active region of QCLs with technological maturity. The technological maturity of such structures is supported in the papers dedicated to the growth accuracy of HgCdTe superlattice [26], intersubband absorption and transition in HgCdTe multiple quantum wells [25,27] and resonant tunneling in HgCdTe heterostructures [28]. $Hg_{0.8}Cd_{0.2}Te/Hg_{0.6}Cd_{0.4}Te$ material system can be grown on (013) GaAs substrate with metamorphic buffer or on $Hg_{0.78}Cd_{0.22}Te$ virtual substrate to satisfy the strain-balance condition. Furthermore, the given $Hg_{0.6}Cd_{0.4}Te$ barrier layer composition is necessary to obtain weak localization of high energy wave function enabling to use highly diagonal radiation transitions.

We analyze three- and two-well designs with resonant-phonon depopulation scheme when the operation bias per period is close to the sum of the emission photon energy 34.3 meV and the longitudinal optical phonon energy 18.3 meV. Our choice of the numbers of wells in the period is motivated by the highest operation temperatures of THz QCLs based on GaAs/AlGaAs with 3-well [29] and 2-well [30] designs. The balance equation method allows us to optimize the chosen HgCdTe-designs in order to achieve the maximum gain for emission frequency of 8.3 THz, varying all barrier layers thicknesses from 1 to 8 nm and well layers thicknesses from 3 to 30 nm with a calculation step equal to half the lattice constant of CdTe ~ 3.25 Å. It is important to note that we focus only on such designs that satisfy the electrical stability condition and have the lowest threshold current.

3. Theoretical model

To calculate the HgCdTe QCL characteristics we have used the balance equation method with "tight-binding" wave-function basis. This basis has been obtained as superposition of eigenstates of the Schrödinger equation for the entire active region of a THz QCL by minimization of the spatial extension of wave functions of tunnel-coupled states. The localized ("tight-binding") basis is more stable for dephasing impact, as degenerate basis states with $\Delta E \lesssim 3$ meV have a small overlap of wavefunctions and, correspondingly, a low self-scattering rate.

The electron levels and wave-functions are calculated via 3-band $\mathbf{k} \cdot \mathbf{p}$ Hamiltonian [24]

$$H = \begin{pmatrix} E_c(z) + p_z \frac{1+2F_K}{2m_0} p_z & \sqrt{\frac{2}{3}} \frac{p_{cv}}{m_0} p_z & -\sqrt{\frac{1}{3}} \frac{p_{cv}}{m_0} p_z \\ -\sqrt{\frac{2}{3}} \frac{p_{cv}}{m_0} p_z & E_{lh}(z) - p_z \frac{\gamma_1+2\gamma_2}{2m_0} p_z & 0 \\ \sqrt{\frac{1}{3}} \frac{p_{cv}}{m_0} p_z & 0 & E_{so}(z) - p_z \frac{\gamma_1}{2m_0} p_z \end{pmatrix} \quad (1)$$

acting on the three-dimensional vector of envelope functions $\psi = (\psi_c, \psi_{vl}, \psi_{so})$. Here $E_c(z)$, $E_{lh}(z)$ and $E_{so}(z)$ are conduction, light-hole and split-off position-dependent band edges, respectively, γ_1 and γ_2 are Luttinger parameters. The momentum matrix element p_{cv} between bulk Bloch states can be presented as $p_{cv} = i\sqrt{m_0 E_p/2}$, where E_p is the Kane energy. For high energy levels it is important to take into account the non-parabolicity of the conduction band. Therefore, the effective Kane parameters for the 3-band $\mathbf{k} \cdot \mathbf{p}$ model are approximated from the dispersion curves obtained in [31,32]. The relevant material parameters for calculations are given in Appendix in Table 1.

The procedure of localization of wave functions are carried out as described in [23]. Then, we calculate the matrix elements of dipole transitions, the probabilities of scattering by optical phonons and impurities, as well as the probability of electron-electron scattering in the approximation of thermodynamic equilibrium. The probability of tunnel junctions are calculated with a random phase approximation using Lorentz line contours. Level populations for one period can be found via system of balanced equations

$$\frac{dn_i}{dt} = -\sum_{j \neq i} \frac{n_i}{\tau_{ij}} + \sum_{j \neq i} \frac{n_j}{\tau_{ji}} - \upsilon_g g_{ij} (n_i - n_j) S - \frac{n_i}{\tau_{\text{esc } i}} = \frac{n_i}{\tau_{\text{esc}}}. \quad (2)$$

Here, τ_{ij} are the times of nonradiative transitions from level i to level j, g_{ij} are differential gains, $\tau_{esc\,i}$ are the electron escape times from localised levels to continuum states, S is the photon surface density in a period and υ_g is the group velocity of light. We calculate $\tau_{esc\,i}$ from the wave-function amplitudes in the continuum, similarly to the lifetimes of optical modes in a cavity.

The current density j_{loc} through the period and the leakage current density j_{leak} is given by [23]

$$j_{loc} (V_1, N_d) = e \sum_{E_i > E_1} \sum_{E_j \leq E_1} \left(\frac{n_i}{\tau_{ij}} - \frac{n_j}{\tau_{ji}} + \upsilon_g g_{ij} (n_i - n_j) S \right), j_{\text{leak}} (V_1, N_d) = e \frac{N_d}{\tau_{\text{esc}}}, \quad (3)$$

where e is the elementary charge and V_1 is the operation bias per period. The total concentration of electrons on the levels equals to the donor concentration N_d.

The contribution of non-resonant transitions has been taken into account to determine the gain spectrum [23,33]

$$G(\nu) = \frac{\pi e^2 h \nu}{\hbar \varepsilon_0 c n_r d} \sum_{E_i > E_j} |z_{ij}|^2 (n_i - n_j) \left[F_{ij} (h\nu, E_i - E_j) - F_{ij} (h\nu, E_j - E_i) \right], \quad (4)$$

where h is the Planck constant, $\hbar = h/2\pi$, ε_0 is the vacuum permittivity, c is the speed of light in vacuum, n_r is the refractive index of the active region, ν is the radiation frequency, d is the

structure period, z_{ij} are dipole matrix elements, n_i and E_i are the surface concentrations of charge carriers and energies of levels i, respectively. The form factor of a spectral line is taken as the form of modified Lorenzian [23]

$$F_{ij}(h\nu, \Delta E) = \frac{\gamma_{ij}}{\pi} \cdot \frac{1}{(h\nu - \Delta E)^2 + \gamma_{ij}^2} \cdot \frac{2}{\left(1 + \exp\left(\frac{h\nu - \Delta E}{kT}\right)\right)\left(1 + \exp\left(-\frac{h\nu + \Delta E}{kT}\right)\right)}. \quad (5)$$

Here, γ_{ij} is the transition linewidth, which takes into account the lifetimes of the corresponding levels. The additional exponential factor, which diminishes the form factor in the short-wavelength spectral region, takes into account the many-body effects of electron-electron interaction, as in [34].

4. Results and discussion

As a result of numerical optimization, we have found the 3-well design with peak gain exceeding of 100 cm^{-1} at a lattice temperature of 150 K. The layer sequence of the single period of optimized design in nanometers **6.5**/11.7/**3.9**/24.0/**2.6**/13.0 with Hg$_{0.6}$Cd$_{0.4}$Te barriers indicated in bold letters and Hg$_{0.8}$Cd$_{0.2}$Te wells, whereas the central part of underlined well is doped with sheet electron density of $6.2 \cdot 10^{10}$cm^{-2}. The band structure and the current flow through the energy levels as simulated by the balance equation method are shown in Fig. 2(a). Electron state 1 of n period and 3 of $n + 1$ period are tunnel-coupled. Taking into account the dephasing effect allows to localize the electron density of basis state 1 mainly in the double quantum well of n period, while the electron density of state 3 is localized in the quantum well of $n + 1$ period. This spatial separation approach of electron densities for tunnel-coupled states has been used in the calculation of the entire active region.

The operation principle of the present design is similar to the conventional 3-well THz QCLs, when the population inversion is based on electron injection into the upper laser level 3 of $n + 1$ period via resonant tunneling from injector level 1 of n period and electron depopulation of the lower laser level 2 of $n + 1$ period occurs with resonant phonon emission landing on the injector level 1 of the same period. This principle is well illustrated by the calculated main current channels through the structure, including the parasitic current channel between the upper laser level 3 and the injector level 1, which are indicated by red arrows. Each red arrow corresponds to the current channel, equal to 251 A/cm^2, and indicates the direction of the current flow. It should also be noted that the present design has an additional resonant phonon extraction mechanism from a high energy level 4 to the upper laser level 3. However, our calculations show that this resonance has a negligible effect on electron transport and, as a result, does not significantly increase the population of the upper laser level 3.

The best temperature robustness is demonstrated by the optimized 2-well design with peak gain exceeding of 100 cm^{-1} at 200 K and layer sequence (in nanometers with barriers in bold letters) **4.5**/5.8/**2.6**/18.8 with a doping density of $3.2 \cdot 10^{10}$ cm^{-2}. As compared with the 3-well design, narrower wells in the 2-well design lead to higher energy levels with weakly localized electron wavefunctions spanning over several periods [see Fig. 2(b)]. Consequently, the 2-well design has a larger spatial overlap of wavefunctions of the laser levels 3 and 2, which increases the dipole matrix element of the radiation transition. On the other hand, utilizing high energy levels in the 2-well design has two detrimental effects. First, the effective mass of the above levels becomes higher due to the non-parabolic band effect. Second, the electron leakage is activated on high energy levels by the parasitic current channel $3 \rightarrow 4$ with sequential tunneling into the continuum.

In the 2-well design the trajectory of the current flow becomes more complex with the main "stream" through laser levels 3 and 2 and the minor current channel based on diagonal transitions between levels 3 and 1, which occur in the direction and opposite to the direction of the current

flow. Furthermore, the present design is characterized by the hybrid injection scheme based on resonant-tunnelling transitions from injector level 1 of n period to upper laser level 3 of $n + 2$ period and scattering-assisted injection from the lower laser level 2 of n period to the upper laser level 3 of $n + 1$ period with resonant emission of optical phonon. In contrast to the 3-well design, the injection mechanism via optical phonon scattering is much more effective in the 2-well design. We emphasize that in the 2-well design the population of the lower laser level 2 is less than the population of the upper laser level 3, since the populations of these levels are related to each other by the Boltzmann distribution $n_2/n_3 \approx \exp\left(-E_{LO}/kT\right)$. Finally, in the 2-well design the parasitic injection from level 1 to the lower laser level 2 is suppressed due to the minimized overlap between wave functions of the corresponding levels. For these reasons, we expect that the 2-well design is less sensitive to the temperature and allows achieving higher operation temperatures than the 3-well design.
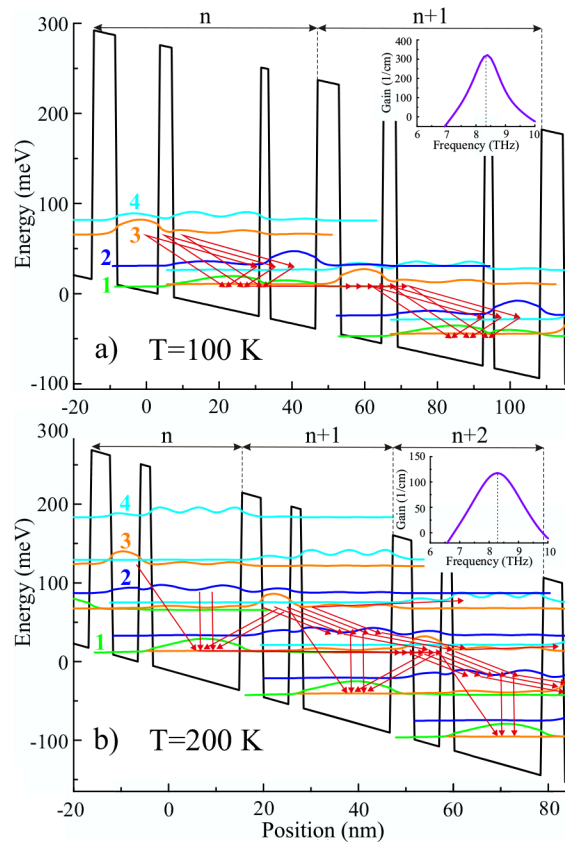
Fig. 2. Conduction band diagram and squared modules of wavefunctions for the $Hg_{0.6}Cd_{0.4}Te/Hg_{0.8}Cd_{0.2}Te$ QCLs computed by 3-band Hamiltonian $\mathbf{k} \cdot \mathbf{p}$-method at a bias of 55 mV/period are demonstrated for (a) two neighboring periods of 3-well design at 100 K and (b) three neighboring periods of 2-well design at 200 K. The red arrows indicate the main current channels through the structure, taking into account that the total current through the period equals to six red arrows for 3-well design (one arrow equals to 251 A/cm²) and nine red arrows for 2-well design (one arrow equals to 272 A/cm²). In the insets, it is possible to see that the gain maximum corresponds to the target frequency of 8.3 THz for both design.

In Fig. 3(a), we compare the calculated current density-voltage and peak gain-voltage characteristics of the optimized 3-well design at two temperatures of 100 K and 150 K. One observes that the operation bias point near 55 mV/period, where the peak gain has a maximum value, is below the peak-current bias at both temperatures. Thus, the present design demonstrates a smooth current-voltage characteristic with operation bias point outside the region of negative differential resistance to prevent electrical instability. It is worth noting that this design has a strong temperature dependence of the current density, which leads to its increasing from 2.8 to 3.8 kA/cm^2 at operation bias point as temperature increases by 50 K. This temperature effect is associated with a $\sim$ 20 % increase of the Bose factor of the electron-phonon scattering rate due to a low optical phonon energy in HgCdTe. In addition, the population of the injector level 1 decreases by 10 %, because the populations of the lower laser level 2 and the high energy level 4 increase by 6 % and 4 %, respectively. As a result, new parasitic channels 4 → 1 and 4 → 2 of current leakage occur at high temperatures. Moreover, with increasing temperature from 100 K to 150 K, the peak gain rapidly drops and the operation bias range shrinks. Thus, the optimized 3-well design depends significantly on temperature and is more suitable for low temperature operation.
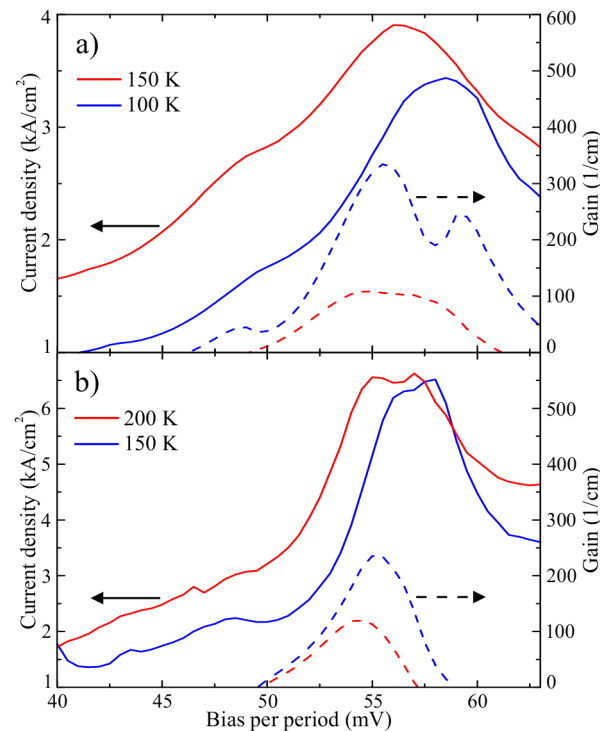
Fig. 3. The current density (solid lines) and peak gain (dashed lines) versus voltage are calculated using the balance equations method for (a) 3-well design at a lattice temperatures of 100 K and 150 K and (b) 2-well design at a lattice temperatures of 150 K and 200 K.

The results of the calculated current density and peak gain versus applied voltage at 150 K and 200 K for the 2-well design are shown in Fig. 3(b). As well as for the 3-well design, the operation bias point near 55 mV/period is on the increasing branch of the current-voltage characteristic. However, we observe that the local gradient of the current-voltage curve of the 2-well design is larger than in the 3-well design. Reasonably, high energy levels of the 2-well design are more sensitive to the applied bias, resulting in a high differential resistance and a narrower operation

bias range. It should also be noted that the current density in the 2-well design is two times higher than in the 3-well design. Therefore, the 2-well design is more suitable for pulsed mode operation to minimize the self-heating effect.

We evaluate the tolerance of optimized designs to a deviation of layer thickness. Our calculations show that the acceptable variation of layer thicknesses for 3-well design is up to ±2 monolayers (±6% of the period thickness). With large deviations from a nominal design, a sharp decrease of peak gain is observed. In case of 2-well design, the thickness tolerance for working lasing structure is determined to be −0.5, +1 monolayer (−2%, +4% of the period thickness). Therefore, the values of acceptable thickness variation for HgCdTe designs are comparable to the growth accuracy requirements for AlGaAs/GaAs based structures [35]. According to [36,37], the mean height of interface roughness of HgCdTe structures is about 0.4-0.5 nm, which is less than the thickness of one monolayer.

In Fig. 4(a), we compare the temperature dependence of the peak gain at 8.3 THz of the optimized 2-well and 3-well designs. At low temperatures, the 3-well design demonstrates the highest peak gain, which begins to decrease rapidly at temperatures above 70 K. Conversely, in case of the 2-well design, the peak gain has lower values with weak temperature dependence up to 150 K and gradually decreases at higher temperatures. This leads to significantly higher peak gain of the 2-well design at temperatures above 120 K and, as a result to higher operating temperatures. In order to estimate the maximum operation temperatures of the given designs, we calculate the cavity losses for a 12 μm thick Cu-Cu waveguide based on HgCdTe as a function of temperature using the method proposed in Ref. [7]. In this case, we take into account scattering on optical phonons [39,40] and free charge carriers [41] for HgCdTe QCL with 75 nm and 50 nm thick n^+-CdTe contact layers with a doping concentration of 10^{17} cm^{-3}. Now we may clearly identify the temperature, which ceases the laser action. Under this temperature the computed optical gain becomes equal to the cavity losses. Such conditions are achieved for the 2-well and 3-well designs at 225 K and 170 K, respectively, which corresponds to the maximum operating temperature of the given designs.

To validate the predictability of our approach, we calculate the temperature dependence of peak gain for the GaAs/AlGaAs QCLs emmiting at THz frequencies with experimental values of maximum operation temperature. We choose the two well-known designs based on 3-well with maximum operation temperature of 142 K [38] and 180 K [29], and the 2-well design with the highest operation temperature of 210.5 K achieved to date [30]. The waveguide parameters of the analyzed QCLs, including the thickness of the contact layers and gain region, doping concentration and cladding metals, are given in Table 2 in the Appendix. As well as for the HgCdTe designs, for the 2-well design based on GaAs/AlGaAs the maximum of peak gain is shifted toward higher temperatures in comparison with the 3-well designs [see Fig. 4(b)]. Furthermore, the peak gain of 2-well design becomes higher than in 3-well designs at temperatures above 120 K, which leads to a higher operation temperature of 2-well design. Finally, we find excellent agreement between the predicted maximum operating temperatures and the experimental values [see Table 2 in the Appendix].

To highlight the difference in the temperature performance of the 2-well and 3-well HgCdTe designs, in Fig. 5 we analyze the main parameters defining the peak gain for both designs as $g_{32} \sim \Delta n_{32} |z_{32}|^2 / \gamma_{32}$, where Δn_{32} is the population inversion, z_{32} is the dipole matrix element, and γ_{32} is the transition linewidth. Despite of the low value of Δn_{32} for the 2-well design, this parameter slightly increases at elevated temperatures and becomes higher than the Δn_{32} of the 3-well at temperatures above 200 K. One more reason of high temperature operation of the 2-well design is a higher value of z_{32}, which increases from 8.8 nm to 9.2 nm with increasing temperature from 50 to 250 K. This can be explained by extended electron wavefunctions of high energy laser levels and the decrease of potential barriers under increasing temperatures. Meanwhile the 3-well design demonstrates a lower value of z_{32}, which is reduced from 6.3 nm
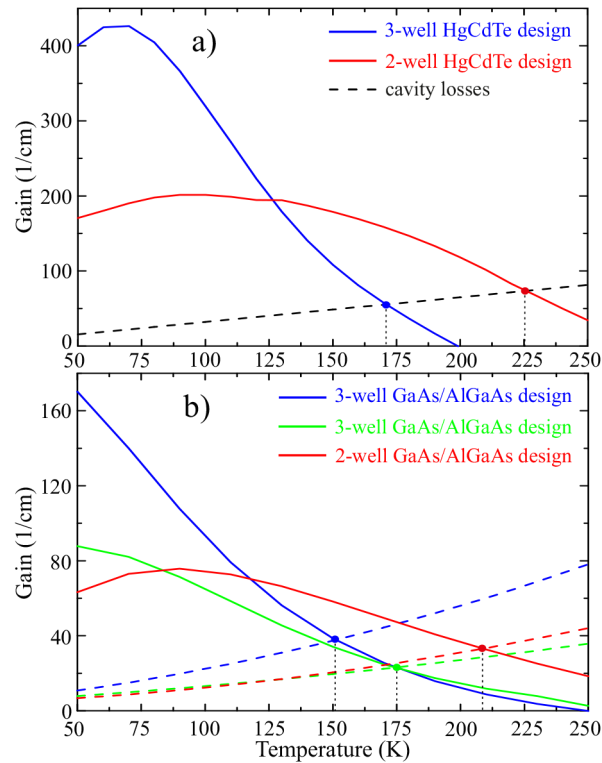
Fig. 4. The temperature dependencies of peak gain are shown for (a) optimized HgCdTe designs based on 3-well (blue line) and 2-well (red line) and (b) GaAs/AlGaAs design based on 3-well of Luo *et al*. [38] (blue line), 3-well of Fathololoumi *et al*. [29] (green line) and 2-well of Bosco *et al*. [30] (red line). Cavity losses are indicated by the dashed curves taking into account the waveguide parameters for each QCL designs shown in Table 2 in the Appendix.

to 6.1 nm within the above temperature range. Thus, the 2-well design has a higher $\Delta n_{32} \cdot z_{32}$ product than the 3-well design at temperatures above 200 K with close γ_{32} for both designs, leading to a higher peak gain and, consequently, to a higher operation temperature.
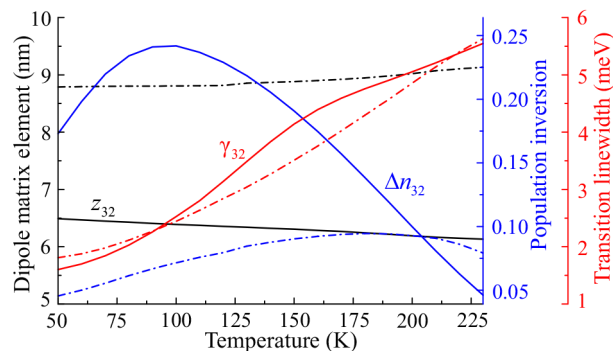
Fig. 5. The temperature dependencies of dipole matrix element z_{32}, population inversion Δn_{32} and transition linewidth γ_{32} are shown for the optimized 3-well (solid curves) and 2-well (dash-dotted curves) designs.

5. Conclusion

In summary, we have demonstrated the potential of the HgCdTe structures as a gain medium for QCL operating in the GaAs phonon Reststrahlen band. Carrier transport and optical gain properties are theoretically investigated using the balance equations method with a 3-band $\mathbf{k} \cdot \mathbf{p}$ Hamiltonian. The HgCdTe active region is optimized by varying of the layer thicknesses in the wide range in order to achieve the maximum gain for emission frequency of 8.3 THz. Finally, we have proposed the three- and two-well designs with maximum operation temperatures of 170 K and 225 K, respectively. We believe that the HgCdTe structures can be a promising candidate for QCLs operating in the frequency range from 7 to 10 THz.

Appendix

Table 1. Relevant material parameters adopted in in this work to simulate the $Hg_{0.8}Cd_{0.2}Te/Hg_{0.6}Cd_{0.4}Te$ QCL systems, $T = 200$ K.

	$Hg_{0.8}Cd_{0.2}Te$	$Hg_{0.6}Cd_{0.4}Te$
Electron effective masses (m_e^*/m_0)	0.011	0.031
Energy bandgap (eV)	0.121	0.424
Spin-orbit splitting (meV)	1046	1012
Effective Kane energy E_p (eV)	15.7	17.6
Effective Kane parameter F_K	−0.45	−0.30
Luttinger parameter γ_1	3.57	3.048
Luttinger parameter γ_2	0.344	0.188
Barrier/well band offset (meV)		252
Static dielectric constant	17.6	15.2
High-frequency dielectric constant	12.4	10.6

Table 2. Double metal waveguide parameters for calculation of cavity losses in analyzed QCLs.

	3-well design [38]	3-well design [29]	2-well design [30]	2,3-well designs
laser frequency, THz	3.4	3.2	3.9	8.3
well material	GaAs	GaAs	GaAs	$Hg_{0.8}Cd_{0.2}Te$
barrier material	$Al_{0.15}Ga_{0.85}As$	$Al_{0.15}Ga_{0.85}As$	$Al_{0.25}Ga_{0.75}As$	$Hg_{0.6}Cd_{0.4}Te$
metal	Au	Au	Cu	Cu
n^+ contact layers, nm / 10^{18}cm^{-3}	50 / 5	50 / 5	50 / 5	50 / 0.1
gain region, μm / 10^{16}cm^{-3}	10 / 0.81	10 / 0.68	12 / 1.5	12 / 1.0
n^+ contact layers, nm / 10^{18}cm^{-3}	400 / 3	75 / 5	0	75 / 0.1
metal	Au	Au	Cu	Cu
T_{max}, K, *experiment*	142	180	210.5	–
T_{max}, K, *theory*	150	175	210	225, 170

Funding

Acknowledgments

Disclosures

The authors declare that there are no conflicts of interest related to this article.

References

1. M. S. Vitiello, G. Scalari, B. Williams, and P. D. Natale, "Quantum cascade lasers: 20 years of challenges," Opt. Express **23**(4), 5167–5182 (2015).
2. Z. Loghmari, M. Bahriz, A. Meguekam, R. Teissier, and A. N. Baranov, "InAs-based quantum cascade lasers emitting close to 25 μm," Electron. Lett. **55**(3), 144–146 (2019).
3. K. Ohtani, M. Beck, M. J. Suess, J. Faist, A. M. Andrews, T. Zederbauer, H. Detz, W. Schrenk, and G. Strasser, "Far-infrared quantum cascade lasers operating in the AlAs phonon reststrahlen band," ACS Photonics **3**(12), 2280–2284 (2016).
4. M. Wienold, B. Roben, X. Lu, G. Rozas, L. Schrottke, K. Biermann, and H. T. Grahn, "Frequency dependence of the maximum operating temperature for quantum-cascade lasers up to 5.4 THz," Appl. Phys. Lett. **107**(20), 202101 (2015).
5. K. Feng, W. Streyer, Y. Zhong, A. Hoffman, and D. Wasserman, "Photonic materials, structures and devices for Reststrahlen optics," Opt. Express **23**(24), A1418–A1433 (2015).
6. Y. J. Han, L. H. Li, J. Zhu, A. Valavanis, J. R. Freeman, L. Chen, M. Rosamond, P. Dean, A. G. Davies, and E. H. Linfield, "Silver-based surface plasmon waveguide for terahertz quantum cascade lasers," Opt. Express **26**(4), 3814–3827 (2018).
7. D. V. Ushakov, A. A. Afonenko, A. A. Dubinov, V. I. Gavrilenko, I. S. Vasilevskii, N. V. Shchavruk, D. S. Ponomarev, and R. A. Khabibullin, "Mode loss spectra in THz quantum-cascade lasers with gold- and silver-based double metal waveguides," Quantum Electron. **48**(11), 1005–1008 (2018).
8. M. Dyksik, M. Motyka, W. Rudno-Rudzinski, G. Sek, J. Misiewicz, D. Pucicki, K. Kosiel, I. Sankowska, J. Kubacka-Traczyk, and M. Bugajski, "Optical properties of active regions in terahertz quantum cascade lasers," J. Infrared, Millimeter, Terahertz Waves **37**(7), 710–719 (2016).
9. T. Grange, D. Stark, G. Scalari, J. Faist, L. Persichetti, L. Di Gaspare, M. De Seta, M. Ortolani, D. J. Paul, G. Capellini, S. Birner, and M. Virgilio, "Room temperature operation of n-type Ge/SiGe terahertz quantum cascade lasers predicted by non-equilibrium Green's functions," Appl. Phys. Lett. **114**(11), 111102 (2019).
10. C. Ciano, M. Virgilio, L. Bagolini, L. Baldassarre, A. Pashkin, M. Helm, M. Montanari, L. Persichetti, L. D. Gaspare, G. Capellini, D. J. Paul, G. Scalari, J. Faist, M. D. Seta, and M. Ortolani, "Terahertz absorption-saturation and emission from electron-doped germanium quantum wells," Opt. Express **28**(5), 7245–7258 (2020).
11. E. Bellotti, K. Driscoll, T. D. Moustakas, and R. Paiella, "Monte Carlo simulation of terahertz quantum cascade laser structures based on wide-bandgap semiconductors," J. Appl. Phys. **105**(11), 113103 (2009).
12. H. Yasuda, T. Kubis, I. Hosako, and K. Hirakawa, "Non-equilibrium Green's function calculation for GaN-based terahertz-quantum cascade laser structures," J. Appl. Phys. **111**(8), 083105 (2012).
13. E. Benveniste, A. Vasanelli, A. Delteil, J. Devenson, R. Teissier, A. Baranov, A. M. Andrews, G. Strasser, I. Sagnes, and C. Sirtori, "Influence of the material parameters on quantum cascade devices," Appl. Phys. Lett. **93**(13), 131108 (2008).
14. S. Ruffenach, A. Kadykov, V. V. Rumyantsev, J. Torres, D. Coquillat, D. But, S. S. Krishtopenko, C. Consejo, W. Knap, S. Winnerl, M. Helm, M. A. Fadeev, N. N. Mikhailov, S. A. Dvoretskii, V. I. Gavrilenko, S. V. Morozov, and F. Teppe, "HgCdTe-based heterostructures for terahertz photonics," APL Mater. **5**(3), 035503 (2017).
15. A. Rogalski, "HgCdTe infrared detector material: history, status and outlook," Rep. Prog. Phys. **68**(10), 2267–2336 (2005).
16. S. V. Morozov, V. V. Rumyantsev, M. A. Fadeev, M. S. Zholudev, K. E. Kudryavtsev, A. V. Antonov, A. M. Kadykov, A. A. Dubinov, N. N. Mikhailov, S. A. Dvoretsky, and V. I. Gavrilenko, "Stimulated emission from HgCdTe quantum well heterostructures at wavelengths up to 19.5 μm," Appl. Phys. Lett. **111**(19), 192101 (2017).
17. M. A. Fadeev, V. V. Rumyantsev, A. M. Kadykov, A. A. Dubinov, A. V. Antonov, K. E. Kudryavtsev, S. A. Dvoretskii, N. N. Mikhailov, V. I. Gavrilenko, and S. V. Morozov, "Stimulated emission in the $2.8 - 3.5$ μm wavelength range from Peltier cooled HgTe/CdHgTe quantum well heterostructures," Opt. Express **26**(10), 12755–12760 (2018).
18. S.-C. Lee and A. Wacker, "Theoretical analysis of spectral gain in a terahertz quantum-cascade laser: Prospects for gain at 1 THz," Appl. Phys. Lett. **83**(13), 2506–2508 (2003).
19. C. Jirauschek, "Density matrix Monte Carlo modeling of quantum cascade lasers," J. Appl. Phys. **122**(13), 133105 (2017).
20. H. Callebaut and Q. Hu, "Importance of coherence for electron transport in terahertz quantum cascade lasers," J. Appl. Phys. **98**(10), 104505 (2005).

21. S. Kumar and Q. Hu, "Coherence of resonant-tunneling transport in terahertz quantum-cascade lasers," Phys. Rev. B **80**(24), 245316 (2009).

22. R. Khabibullin, N. Shchavruk, D. Ponomarev, D. Ushakov, A. Afonenko, K. Maremyanin, O. Volkov, V. Pavlovskiy, and A. Dubinov, "The operation of THz quantum cascade laser in the region of negative differential resistance," Opto-Electron. Rev. **27**(4), 329–333 (2019).

23. D. Ushakov, A. Afonenko, A. Dubinov, V. Gavrilenko, O. Volkov, N. Shchavruk, D. Ponomarev, and R. Khabibullin, "Balance-equation method for simulating terahertz quantum-cascade lasers using a wave-function basis with reduced dipole moments of tunnel-coupled states," Quantum Electron. **49**(10), 913–918 (2019).

24. C. Sirtori, F. Capasso, J. Faist, and S. Scandolo, "Nonparabolicity and a sum rule associated with bound-to-bound and bound-to-continuum intersubband transitions in quantum wells," Phys. Rev. B **50**(12), 8663–8674 (1994).

25. A. M. de Paula, C. R. M. de Oliveira, G. E. Marques, A. M. Cohen, R. D. Feldman, R. F. Austin, M. N. Islam, and C. L. Cesar, "Interband and intersubband absorption in HgCdTe multiple quantum wells," Phys. Rev. B **59**(15), 10158–10164 (1999).

26. Z. Yang, Z. Yu, Y. Lansari, S. Hwang, J. W. Cook, and J. F. Schetzina, "Optical properties of HgTe/CdTe superlattices in the normal, semimetallic, and inverted-band regimes," Phys. Rev. B **49**(12), 8096–8108 (1994).

27. C. R. M. de Oliveira, A. M. de Paula, C. L. Cesar, L. C. West, C. Roberts, R. D. Feldman, R. F. Austin, M. N. Islam, and G. E. Marques, "Photoinduced intersubband transition in undoped HgCdTe multiple quantum wells," Appl. Phys. Lett. **66**(22), 2998–3000 (1995).

28. M. A. Reed, R. J. Koestner, M. W. Goodwin, and H. F. Schaake, "Resonant tunneling in HgCdTe heterostructures," J. Vac. Sci. Technol., A **6**(4), 2619–2622 (1988).

29. S. Fathololoumi, E. Dupont, C. Chan, Z. Wasilewski, S. Laframboise, D. Ban, A. Mátyás, C. Jirauschek, Q. Hu, and H. C. Liu, "Terahertz quantum cascade lasers operating up to ∼ 200 K with optimized oscillator strength and improved injection tunneling," Opt. Express **20**(4), 3866–3876 (2012).

30. L. Bosco, M. Franckie, G. Scalari, M. Beck, A. Wacker, and J. Faist, "Thermoelectrically cooled THz quantum cascade laser operating up to 210 K," Appl. Phys. Lett. **115**(1), 010601 (2019).

31. M. T. Czyżyk and M. Podgórny, "Energy bands and optical properties of HgTe and CdTe calculated on the basis of the tight-binding model with spin–orbit interaction," Phys. Status Solidi B **98**(2), 507–516 (1980).

32. L. S. Bovkun, A. V. Ikonnikov, V. Y. Aleshkin, K. E. Spirin, V. I. Gavrilenko, N. N. Mikhailov, S. A. Dvoretskii, F. Teppe, B. A. Piot, M. Potemski, and M. Orlita, "Landau level spectroscopy of valence bands in HgTe quantum wells: effects of symmetry lowering," J. Phys.: Condens. Matter **31**(14), 145501 (2019).

33. B. Gelmont, V. Gorfinkel, and S. Luryi, "Theory of the spectral line shape and gain in quantum wells with intersubband transitions," Appl. Phys. Lett. **68**(16), 2171–2173 (1996).

34. A. Afonenko and V. Kononenko, "Spectral line broadening in quantum wells due to Coulomb interaction of current carriers," Phys. E (Amsterdam, Neth.) **28**(4), 556–567 (2005).

35. A. E. Yachmenev, S. S. Pushkarev, R. R. Reznik, R. A. Khabibullin, and D. S. Ponomarev, "Arsenides-and related III-V materials-based multilayered structures for terahertz applications: Various designs and growth technology," Prog. Cryst. Growth Charact. Mater. **66**(2), 100485 (2020).

36. S. Dvoretsky, N. Mikhailov, V. Remesnik, Y. Sidorov, V. Shvets, D. Ikusov, V. Varavin, M. Yakushev, J. Gumenjuk-Sichevska, A. Golenkov, I. Lysiuk, Z. Tsybrii, A. Shevchik-Shekera, F. Sizov, A. Latyshev, and A. Aseev, "MBE-grown MCT hetero- and nanostructures for IR and THz detectors," Opto-Electron. Rev. **27**(3), 282–290 (2019).

37. N. Mikhailov, V. Shvets, D. Ikusov, I. Uzhakov, S. Dvoretsky, K. Mynbaev, P. Dluzewski, J. Morgiel, Z. Swiatek, O. Bonchyk, and I. Izhnin, "Interface studies in HgTe/HgCdTe quantum wells," Phys. Status Solidi B **257**(5), 1900598 (2020).

38. H. Luo, S. R. Laframboise, Z. R. Wasilewski, G. C. Aers, H. C. Liu, and J. C. Cao, "Terahertz quantum-cascade lasers based on a three-well active module," Appl. Phys. Lett. **90**(4), 041112 (2007).

39. J. Baars and F. Sorger, "Reststrahlen spectra of HgTe and $Cd_xHg_{1-x}Te$," Solid State Commun. **10**(9), 875–878 (1972).

40. M. Grynberg, R. Le Toullec, and M. Balkanski, "Dielectric function in HgTe between 8 and 300 K," Phys. Rev. B **9**(2), 517–526 (1974).

41. J. A. Mroczkowski and D. A. Nelson, "Optical absorption below the absorption edge in $Hg_{1-x}Cd_xTe$," J. Appl. Phys. **54**(4), 2041–2051 (1983).